Thin-wire Models for Inclined Conductors with Frequency-dependent Losses

Binghao Li, Yaping Du and Mingli Chen

Dept. of Building Services Engineering, The Hong Kong Polytechnic University
Hung Hom, Kowloon, Hong Kong

***Abstract* — This paper presents the FDTD thin-wire models of lossy wire structures with arbitrary inclination for transient analysis, which is difficult to address using traditional FDTD methods. The frequency-dependent losses of the conductors are fully taken into account, and the vector fitting technique is applied to deal with frequency-dependent parameters for time-domain analysis. The bidirectional coupling within the lossy coaxial conductors is modelled. The currents in inner and outer conductors are not necessarily balanced. Three cases are presented for the investigation of wave propagation velocity, wave attenuation, and current distribution. These data are compared with analytical results and numerical results using other models. It is found that the proposed thin-wire models can depict the transient behaviors in the lossy inclined conductors with the velocity error of less than 1%, and the attenuation error of less than 1.5%.**

***Keywords* — finite-difference time-domain (FDTD), thin-wire model, inclination, frequency-dependent loss**

I. Introduction

Wire structures are widely used in industry for engineering systems, ranging from large scale integrated circuits (micrometer-level) through metallic pipelines and beams in buildings (meter-level) to overhead lines and buried cables (kilometer-level). They are the essential elements in estimating electromagnetic (EM) transients during normal and abnormal system operations. The finite-difference time-domain (FDTD) method [1] is one of the commonly-used numerical methods for wire structure modelling and transient simulation. This method has advantages of easy programming and understanding, broadband frequency response, matrix free and parallel computing. Thanks to the thin-wire modelling techniques developed recently [2-5], wire structures can be constructed in a coarse FDTD mesh to reduce computation time and memory space in simulations. Such techniques have been successfully applied to analyze EM transients in electric power systems, such as grounding systems [6], high voltage substations [7, 8], overhead lines [9-15], transmission towers [16-18], vertical conductors [19-21], wind turbine generator systems [22], electrical wirings in buildings [23] and electrified railway systems [24].

The thin-wire modelling techniques can be classified in two groups: 1) sub-cell method, and 2) separated domain method. The sub-cell method builds an equivalent thin-wire structure with effective cell parameters in the FDTD mesh. These effective parameters are obtained either analytically [3, 5] or numerically [4]. This group of thin-wire techniques is straightforward, easily implemented and less time consuming. With these techniques, a series of extended thin-wire models have been proposed for coaxial conductors considering frequency-dependent losses [21, 25] and conductors with non-circular cross sections [24]. Note that thin-wire structures must attach to the FDTD edges. The zig-zag path arrangement for inclined conductors will induce a slower propagation speed as a result of the staircase approximation [26].

The thin-wire modelling techniques [2] based on the separated domain method construct thin-wire models in an additional domain. Two domains, coupled by the in-cell inductance technique, are independent. As a result, this group of thin-wire models has the potential to simulate transients in inclined conductors with desirable performance [27-30]. With these techniques, an insulated wire model [31] and a coaxial conductor model [32] have been proposed recently. However, the frequency-dependent characteristic of the inclined conductors was not taken into account. In addition, the bidirectional coupling between core and sheath conductors, as well as eddy current in the sheath conductor were not considered in the existing model for inclined conductors [32].

This paper presents a series of FDTD thin-wire models for inclined conductors considering frequency-dependent losses, including solid conductors, hollow tubes and coaxial conductors. In the model for coaxial conductors, the bidirectional coupling between the core and sheath conductors, and the eddy current in the sheath conductor are modeled. The currents in both core and sheath conductors are not necessarily balanced. Frequency-dependent parameters of the conductors are expressed first with the Bessel functions, then are approximated by the vector fitting technique for time-domain analysis. Section II reviews the fundamentals of the traditional inclined thin-wire model. Thin-wire models considering frequency-dependent losses are addressed in Section III and IV. In Section V, three case studies are presented for validating the proposed thin-wire models and investigating lightning transients in the wire systems.

II. Traditional Inclined Thin-wire Model

In the thin-wire model [2] proposed by Holland and Simpson, a conductor is posited in the thin-wire domain. As this domain is separated from the normal FDTD domain, it is possible to simulate an inclined configuration with this model.

The wave propagation along the conductor is updated with auxiliary equations. Both current I and charge Q on the conductor are used as updating variables. For handling multi-wire junctions charge Q is substituted with virtual

voltage V, i.e. $V = Q/C$. Assume that the length of a conductor is much longer than its radius, and the EM field near the conductor is quasi-static. The auxiliary updating equations of the thin-wire model in the thin-wire domain can be then represented as,

$$\langle L\rangle \cdot \frac{\partial I}{\partial t} + \frac{\partial V}{\partial l} = \langle E_l\rangle - E_s \tag{1a}$$

$$\langle C\rangle \cdot \left(\frac{\partial \mathrm{V}}{\partial t} + \frac{\sigma}{\varepsilon} V\right) + \frac{\partial I}{\partial l} = 0, \tag{1b}$$

where E_s denotes the surface electric field of the conductor. $\langle E_l\rangle$ is the averaged electric field near the conductor. $\langle L\rangle$ denotes the in-cell inductance. $\langle x\rangle$ means the parameter obtained by an interpolated and synthesized procedure. Note that the capacitance $\langle C\rangle$ is determined by in-cell inductances of two neighboring segments as,

$$\langle C\rangle = \left(\frac{1}{\langle L_+\rangle} + \frac{1}{\langle L_-\rangle}\right) \cdot \frac{\varepsilon\mu\Delta l}{2}, \tag{2}$$

where Δl is the length of line segments for the conductor.

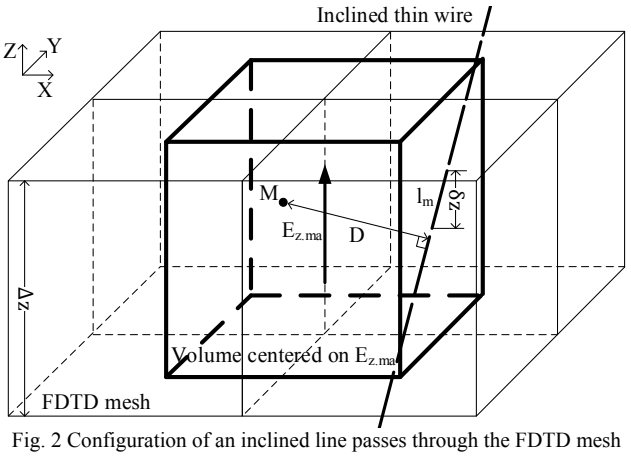

Fig. 2 Configuration of an inclined line passes through the FDTD mesh

In the thin-wire domain, the conductor is divided into a series of line segments. Both voltage V and charge Q are located at line segment centers and edges, respectively. For a segment passes through an FDTD cell, it is surrounded by 12 E field components positing on the 12 cubic cell edges, i.e. 4 E components in each of x, y and z directions. The in-cell inductance of a segment is synthesized by 12 sub-inductances associated with these 12 components. Fig. 1 shows the configuration of segment l_m, and field component E_z. Denote subscript a the index of 4 E components in the z direction. Volume $V_{z.ma}$ (a=1, 2, 3 and 4) is then formed with the center on $E_{z.ma}$, and is depicted as a cubic with thicker lines in Fig. 1. The sub-inductance in the z direction between segment l_m and $V_{z.ma}$ is calculated by,

$$\langle L_{z.ma}\rangle = \frac{\mu \iiint_{V_{z.ma}} \ln\left(D(x,y,z)/r_0\right) dxdydz}{2\pi\Delta x\Delta y\Delta z}, \tag{3}$$

where r_0 is the thin-wire radius, Δx, Δy and Δz are the cell sizes of the FDTD mesh. D is the radial length between the point M in the volume $V_{z.ma}$ and the inclined conductor. Then, the inductance in the z direction can be interpolated with 4 sub-inductances with the trilinear interpolation method as,

$$\langle L_{z.m}\rangle = \sum_{a=1}^{4} \langle L_{z.ma}\rangle \cdot p_{z.ma}, \tag{4}$$

where $p_{z.ma}$ is a weighting coefficient. For sub-inductance L_{zm1}, its coefficient is defined as

$$p_{zm1} = \frac{(\Delta x - \delta x)(\Delta y - \delta y)\delta z}{\Delta x\Delta y\Delta z}, \tag{5}$$

where δx and δy are the protected distances on the xy plane between the segment center to the FDTD cell, as shown in Fig 2. δz denotes the projected length of the line segment in the z direction, as shown in Fig. 1. Finally, the in-cell inductance of line segment l_m are synthesized with the inductances in the x, y and z directions as,

$$\langle L_m\rangle = \sum_{u=x,y,z} \langle L_{um}\rangle \cdot r_u^2, \tag{6}$$

where r_u is the slope of the inclined thin-wire structure in the u (x, y or z) direction.

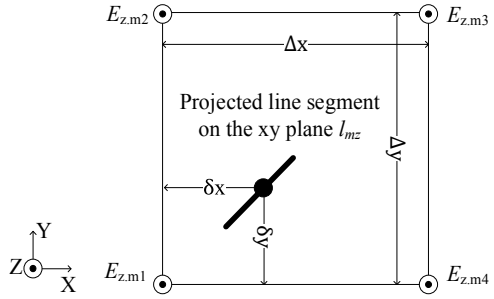

Fig. 2 Relative positions between the projected thin-wire component l_{mz} on the xy plane and four Ez field components

Similar to the in-cell inductance, $\langle E_l\rangle$ is obtained with 12 E field components calculated in the FDTD domain with the interpolating and synthesizing techniques. Conductor current I and virtual voltage V in the thin-wire domain are then updated with the auxiliary equations in (1). At the next half time step, conductor current I is projected in the FDTD domain orientated in x, y and z directions. For each direction, the projected I component is further decomposed into 4 sub-components associated with corresponding E field components using the trilinear method given in (5). As a result, the conductor carrying current is represented as a series of equivalent current sources in the FDTD domain. EM field outside the conductor is updated in the FDTD cells. The procedure of updating both E/H fields and voltage/current is fully described in [30], and is summarized in Fig. 3.

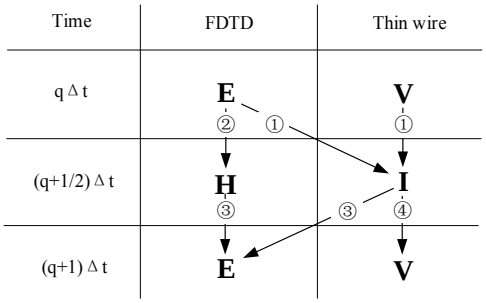

Fig. 3 Calculation procedure of the traditional inclined thin-wire model with auxiliary updating equations

In this procedure, only lossless or conductors with DC loss are considered. The surface electric field E_s is simply equal to either zero or constant voltage drop of IR_{DC}, where R_{DC} is the per-length DC resistance. Both bidirectional coupling between core and sheath conductors, and eddy current in the sheath conductor were not considered.

III. Solid Wires or Hollow Tubes with Frequency-dependent Losses

In a cylindrical conductor with finite conductivity, the surface electric field E_s is non-trivial. It is determined by the product of surface impedance Z and conductor current I in this paper. Note, the surface impedance is frequency-dependent, but can be expressed using Bessel functions [33], as shown in the Appendix. To incorporate the frequency-dependent parameters into the time-domain computation of current I with (1), the surface impedance is approximated with the vector fitting technique [34, 35] as a rational function. The surface electric field E_s in s domain is then expressed as

$$\begin{aligned} E_s(s) &= Z(s)\cdot I(s) \\ &= dI(s) + shI(s) + \sum_{m=1}^{N} \frac{r_m}{s-a_m} I(s), \end{aligned} \tag{7}$$

where d and h represent respectively the constant and differential components, and a_m and r_m are poles and residues of the rational function.

By applying an inverse Laplace transform, the surface electric field, discretized in both time and space with the central difference method, is expressed as

$$\begin{aligned} E_s^{\,q-\frac{1}{2}}(k) = &\left(\frac{d}{2}+\frac{h}{\Delta t}+\frac{1}{2}\sum_{m=1}^{N} B_m\right) I^q(k) + \left(\frac{d}{2}-\frac{h}{\Delta t}\right) I^{q-1}(k) \\ &+ \frac{1}{2}\sum_{m=1}^{N}\left[\left(e^{a_m \Delta t}+1\right)\varphi_m^{q-1}(k)\right] \end{aligned}, \tag{8}$$

where

$$\begin{aligned} B_m &= r_m / a_m \cdot \left(e^{a_m \Delta t}-1\right) \\ \varphi_m^q(k) &= B_m I^q(k) + e^{a_m \Delta t}\varphi_m^{q-1}(k) \end{aligned}.$$

In (1), q denotes the time step, and k denotes the index of a line segment. The last term in the right hand side of (6) is a convolutional term.

Substituting (8) in (1a), the conductor current I considering the frequency-dependent loss in the conductor is obtained as

$$\begin{aligned} I^q(k) = &C_{Is,Is}\cdot I^{q-1}(k) + C_{Is,Vs}\cdot \begin{bmatrix} V^{q-1/2}(k+1/2) \\ -V^{q-1/2}(k-1/2) \end{bmatrix} \\ &+ C_{Is,Es}\cdot\left\{\left\langle E_l^{q-1/2}(k)\right\rangle - \frac{1}{2}\sum_{m=1}^{N}\left[\left(e^{A_m}+1\right)\cdot\varphi_m^{q-1}(k)\right]\right\} \end{aligned} \tag{9}$$

where

$$C_{Is,Is} = \frac{2L - d\Delta t + 2h}{DENO}$$

$$C_{Is,Vs} = -\frac{2\Delta t}{\Delta l \cdot DENO}$$

$$C_{Is,Es} = \frac{2\Delta t}{DENO}$$

$$DENO = 2L + d\Delta t + 2h + \Delta t\sum_{m=1}^{N} B_m$$

The updating equation of the conductor voltage V remains the same as (1b).

IV. Coaxial Conductors with Frequency-dependent Losses

A. Surface electric field of the sheath conductor

The coaxial conductors consist of a core conductor, an insulation gap and a sheath conductor, as shown in Fig. 4. This structure carries both currents I_{co} in the core and I_{sh} in the sheath. These currents may not be necessarily balanced in the simulation. Note that the structure length is much longer than its cross sectional dimensions. Divide the structure into a number of short segments. Electric field on the outer surface of the sheath conductor in segment k can be then expressed with core and sheath currents in frequency domain, as follows:

$$E_s(k) = Z_{c,co}\cdot I_{co}(k) + Z_{c,sh}\cdot I_{sh}(k). \tag{10}$$

where $Z_{c,co}$ and $Z_{c,sh}$ are the surface impedances on the outer sheath surface caused by the core and sheath currents I_{co} and I_{sh}. The detailed expressions of surface impedances are given in the Appendix.

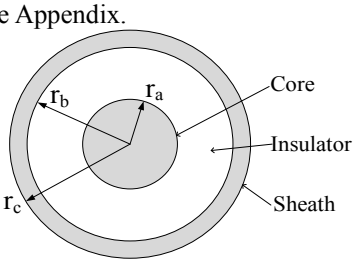

Fig. 4 Cross section of the coaxial conductors

Note that total current I_t of a wire structure is used in the auxiliary equations in (1), instead of I_{co} and I_{sh}. It is necessary to build additional equations in the coaxial wire structures, apart from the auxiliary equations. For a long coaxial wire structure, frequency-domain transmission line equations in discrete form can be established, as follows:

$$\begin{aligned} \frac{V_T(k+1/2)-V_T(k-1/2)}{\Delta l} = &-sL_T I_{co}(k) + Z_{a,sh} I_{sh}(k) \\ &-(Z_{c,co}-Z_{a,co})I_{co}(k) \end{aligned}, \tag{11a}$$

$$\frac{I_{co}(k)-I_{co}(k-1)}{\Delta l} = -sC_T V_T(k-1/2), \tag{11b}$$

$$I_t(k) = I_{co}(k) + I_{sh}(k), \tag{11c}$$

where V_T is the transverse voltage on the gap of the coaxial wire structure, $Z_{a,x}$ and $Z_{b,x}$ (x=*co* or *sh*) are the surface impedances on the core surface and inner sheath surface contributed by the current in conductor x. Both circuit parameters L_T and C_T are given by

$$\begin{aligned} L_T &= \frac{\mu}{2\pi}\ln(r_a / r_c) \\ C_T &= 2\pi\varepsilon \ln^{-1}(r_a / r_c) \end{aligned}. \tag{12}$$

Surface impedances in the lossy conductors are frequency-dependent. Similar to the solid conductors, the vector fitting technique is applied to express surface impedances with rational functions for time-domain simulation, as follows:

$$Z_{a.co}(s) = d_c + sh_c + \sum_{m=1}^{N}\frac{r_{cm}}{s-a_{cm}}, \tag{13a}$$

$$Z_{b,co}(s) = d_{s1} + sh_{s1} + \sum_{m=1}^{N}\frac{r_{s1m}}{s-a_{s1m}}, \tag{13b}$$

$$Z_{b,sh}(s) = d_{s2} + sh_{s2} + \sum_{m=1}^{N} \frac{r_{s2m}}{s - a_{s2m}}, \quad (13c)$$

$$Z_{c,co}(s) = d_{o1} + sh_{o1} + \sum_{m=1}^{N} \frac{r_{o1m}}{s - a_{o1m}}, \quad (13d)$$

$$Z_{c,sh}(s) = d_{o2} + sh_{o2} + \sum_{m=1}^{N} \frac{r_{o2m}}{s - a_{o2m}}. \quad (13e)$$

By substituting (11c) in (11a) and (11b), and taking an inverse Laplace transform, both discrete core current and gap voltage in the time domain can be expressed with the total current I_t, as follows:

$$I_{co}^{q}(k) = C_{Ic,Ic} I_{co}^{q-1}(k) + C_{Ic,Itp} I_t^{q}(k) + C_{Ic,Itn} I_t^{q-1}(k) + C_{Ic,\varphi} \psi_{co}^{q-1}(k) + C_{Ic,V_T} \begin{bmatrix} V_T^{q-1/2}(k+1/2) \\ -V_T^{q-1/2}(k-1/2) \end{bmatrix}, \quad (14a)$$

$$V_T^{q+1/2}(k-1/2) = V_T^{q-1/2}(k-1/2) + C_{V_T,Ic} \begin{bmatrix} I_{co}^{q}(k) \\ -I_{co}^{q}(k-1) \end{bmatrix}, \quad (14b)$$

where

$$C_{Ic,Ic} = -\left(\frac{d_c - d_{s1} + d_{s2}}{2} + \frac{L_T + h_c - h_{s1} + h_{s2}}{\Delta t} \right) \Big/ DENO_{co}$$

$$C_{Ic,Itp} = \left(\frac{d_{s2}}{2} + \frac{h_{s2}}{\Delta t} + \frac{1}{2} \sum_{m=1}^{N} B_{s2m} \right) \Big/ DENO_{co}$$

$$C_{Ic,Itn} = \left(\frac{d_{s2}}{2} - \frac{h_{s2}}{\Delta t} \right) \Big/ DENO_{co}$$

$$C_{Ic,V_T} = -1 \big/ \left(\Delta l \cdot DENO_{co} \right)$$

$$C_{Ic,\varphi} = -1 / (2 \cdot DENO_{co})$$

$$DENO_{co} = \frac{d_c - d_{s1} + d_{s2}}{2} + \frac{L_T + h_c - h_{s1} + h_{s2}}{\Delta t} + \frac{1}{2} \sum_{m=1}^{N} \left(B_{cm} - B_{s1m} + B_{s2m} \right)$$

$$C_{V_T,Ic} = -\Delta t / \Delta l / C_T$$

$$\psi_{co}^{q-1}(k) = \sum_{m=1}^{N} \begin{bmatrix} \left(e^{a_{cm} \cdot \Delta t} + 1 \right) \varphi_{co.cm}^{q-1} - \left(e^{a_{s1m} \cdot \Delta t} + 1 \right) \varphi_{co.s1m}^{q-1} \\ + \left(e^{a_{s2m} \cdot \Delta t} + 1 \right) \varphi_{co.s2m}^{q-1} - \left(e^{a_{s2m} \cdot \Delta t} + 1 \right) \varphi_{t.s2m}^{q-1} \end{bmatrix}$$

$$\varphi_{co.xm}^{q}(k) = B_{xm} \cdot I_{co}^{q}(k) + e^{a_{xm} \cdot \Delta t} \cdot \varphi_{co.xm}^{q-1}(k)$$

$$\varphi_{t.xm}^{q}(k) = B_{xm} \cdot I_t^{q}(k) + e^{a_{xm} \cdot \Delta t} \cdot \varphi_{t.xm}^{q-1}(k)$$

$$B_{xm} = \frac{r_{xm}}{a_{xm}} \left(e^{a_{xm} \cdot \Delta t} - 1 \right)$$

With (11c) and (14a), electric field E_s on the outer surface of the sheath E_s in (10) can be estimated as

$$E_s^{q-1/2}(k) = C_{It,Itn} I_t^{q}(k) + C_{It,Itp} I_t^{q-1}(k) + C_{It,Icp} I_{co}^{q-1}(k) + C_{Es,Icp} C_{Ic,V_T} \begin{bmatrix} V_T^{q-1/2}(k+1/2) - \\ V_T^{q-1/2}(k-1/2) \end{bmatrix} + C_{Ic,\varphi} \psi_{co}^{q-1} / 2 + C_{Es,\varphi} \psi_{Es}^{q-1} \quad (15)$$

where

$$I_t(k) = I_{co}(k) + I_{sh}(k)$$

$$C_{It,Itn} = C_{Es,Icp} C_{Ic,Itp} + C_{Es,Itp}$$

$$C_{It,Itp} = C_{Es,Icp} C_{Ic,Itn} + C_{Es,Itn}$$

$$C_{It,Icp} = C_{Es,Icp} C_{Ic,Ic} + C_{Es,Icn}$$

$$C_{Es,Icp} = \frac{d_{o1} - d_{o2}}{2} + \frac{h_{o1} - h_{o2}}{\Delta t} + \frac{1}{2} \sum_{m=1}^{N} \left(B_{o1m} - B_{o2m} \right)$$

$$C_{Es,Icn} = \frac{d_{o1} - d_{o2}}{2} + \frac{h_{o1} - h_{o2}}{\Delta t}$$

$$C_{Es,Itp} = \frac{d_{o2}}{2} + \frac{h_{o2}}{\Delta t} + \frac{1}{2} \sum_{m=1}^{N} B_{o2m}$$

$$C_{Es,Itn} = \frac{d_{o2}}{2} + \frac{h_{o2}}{\Delta t}$$

$$\psi_{Es}^{q-1} = \sum_{m=1}^{N} \begin{bmatrix} \left(e^{a_{o1m} \cdot \Delta t} + 1 \right) \varphi_{co.o1m}^{q-1} - \left(e^{a_{o2m} \cdot \Delta t} + 1 \right) \varphi_{co.o2m}^{q-1} \\ + \left(e^{a_{o2m} \cdot \Delta t} + 1 \right) \varphi_{t.o2m}^{q-1} \end{bmatrix}$$

B. Current distribution in the coaxial conductors

To update the field components in the FDTD domain, the total wire structure current I_t needs to be determined. Substituting the surface electric field given in (15) into the discrete version of auxiliary equations in (1a) yields I_t in the time domain as

$$I_t^{q}(k) = C_{It,It} \cdot I_t^{q-1}(k) + C_{It,Ic} \cdot I_{co}^{q-1}(k) + C_{It,V_T} \cdot \left[V_T^{q-1/2}(k+1/2) - V_T^{q-1/2}(k-1/2) \right] + C_{It,Vs} \cdot \left[V^{q-1/2}(k+1/2) - V^{q-1/2}(k-1/2) \right] + \psi_t^{q-1} + C_{It,E_l} \cdot \left\langle E_l^{q-1/2}(k) \right\rangle, \quad (16)$$

where

$$C_{It,It} = \left(\langle L \rangle / \Delta t - C_{Es,Icp} \cdot C_{Ic,Itn} - C_{Es,Itn} \right) \Big/ DENO_t$$

$$C_{It,Ic} = -\left(C_{Es,Icp} \cdot C_{Ic,Ic} + C_{Es,Icn} \right) \Big/ DENO_t$$

$$C_{It,V_T} = -C_{Es,Icp} \cdot C_{Ic,V_T} / DENO_t$$

$$C_{It,Vs} = -1 / (\Delta d \cdot DENO_t)$$

$$C_{It,E_l} = 1 / DENO_t$$

$$\psi_t^{q-1}(k) = -\left(C_{Es,Icp} \cdot C_{Ic,\varphi} \cdot \psi_{co}^{q-1}(k) + C_{Es,\varphi} \cdot \psi_{Es}^{q-1}(k) \right) \Big/ DENO_t$$

$$DENO_t = \langle L \rangle / \Delta t + C_{Es,Icp} \cdot C_{Ic,Itp} + C_{Es,Itp}$$

Both core and sheath currents I_{co} and I_{sh} are then calculated with (14a) and (11c) after the total structure current I_t is obtained.

C. Boundary conditions for the coaxial conductors

At each end of a wire structure, the current continuity is enforced by a multi-junction equation in [30] no matter whether there is any external wire connected or not. Additional equations must be established to include gap voltage at the end of the coaxial wire structure for updating FDTD field components.

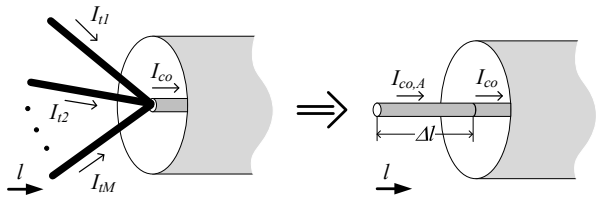

(a) Multi-wire connection (b) Virtual wire connection

Fig. 5 The structure of multi-junctions at coaxial conductor terminal

Fig. 5 illustrates the arrangement of M external wires connected to the core of a coaxial wire structure. A virtual wire segment of length Δl is added to the end of the core

conductor as the representation of the external wires, as shown in Fig. 5(b). This wire segment carries the total current of all external wires, as follows:

$$I_{co,A}^{q} = \sum_{m=1}^{M} I_{tm}^{q} \tag{17}$$

With (11b), the gap voltage at the end of the coaxial conductors can be obtained with the currents in the virtual core segment and its adjacent segment. The updating equation for the gap voltage V_A at the end shown in Fig. 5 is derived as

$$V_{T,A}^{q+1/2} = V_{T}^{q-1/2} + C_{V_T,Ic} \cdot \left[I_{co}^{q}(1) - I_{co,A} \right] \tag{18}$$

The updating equation at other ends of the wire structure can be derived in a similar manner. In case the core is open at the end of the wire structure, I_{co} is simply set to be zero.

The gap voltage, existing at the end of the coaxial wire structure, will alter EM field in its vicinity in the FDTD cells. To establish a link between the voltage at the end and its surrounding EM field, two orthogonal sets of double square surfaces are constructed at the structure end along the wire axis, as shown in Fig. 6. The size of these surfaces is equal to segment length of the conductors. The Faraday's law is then applied in each surface for evaluating H field components in these areas, as follows:

$$\begin{aligned} H_{s1} &= H_{s4} = \frac{dt}{\mu \cdot \Delta l^2} \cdot V_{T,A} \\ H_{s2} &= H_{s3} = -\frac{dt}{\mu \cdot \Delta l^2} \cdot V_{T,A} \end{aligned} \tag{19}$$

where H_{si} is the averaged magnetic field on the corresponding surface S_i. In the normal FDTD updating cycle of magnetic fields, H field components calculated with (18) are interpolated and superposed to the FDTD magnetic field components in the corresponding FDTD cells.

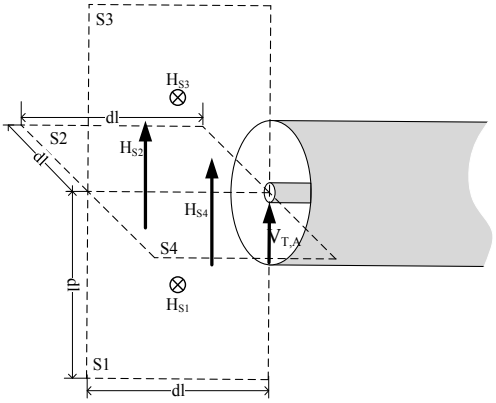

Fig. 6 Configuration for evaluating magnetic fields at the structure end

D. Flow chart

The calculation flow chat of the proposed thin-wire model is illustrated in Fig. 7. The detailed procedure is summarized, as follows:

1) Update electric field component E in the FDTD domain using I_t and H;
2) Update virtual voltage V in the thin-wire domain with (1b) using I_t;
3) Update gap voltage V_T at the end of the coaxial conductors with (14b) using I_{co};
4) Update total current I_t with (16) using I_{co}, E, V and V_T;
5) Update core conductor current I_{co} inside the coaxial wire structure with (14a) using V_T and I_t. If necessary, update sheath conductor current I_{sh} with (11c) using I_t and I_{co};
6) Update magnetic field component H in the FDTD domain with (19) using V_T and E.

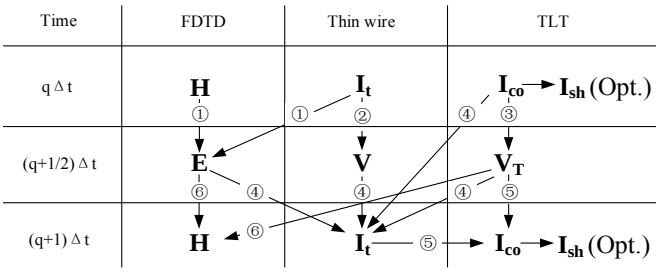

Fig. 7 Calculation procedure of the proposed thin-wire model for coaxial conductors

V. CASE STUDIES

The proposed thin-wire models for inclined lossy conductors are tested under transient or wave propagating conditions in this section. The issues of propagation velocity and frequency-dependent losses on the conductors are investigated. The simulation results are compared with those obtained by analytical and numerical methods for validation.

A. Propagation velocity

The wave propagation velocity of the proposed thin-wire model is tested first. Fig. 8 shows the configuration of a dipole structure with a voltage source located between two conductive arms [26]. The length and radius of each conductive arm are 1 m and 0.1 mm, respectively. The conductivity of two arms is 5.96e7 S/m. The voltage source at the feeding point generates a Gaussian impulse expressed by

$$V(t) = A_0 \exp\left[-\frac{1}{2}\left(\frac{t-\mu}{\sigma} \right)^2 \right], \tag{20}$$

where $A_0 = 1\text{V}$, $\sigma = 1 \times 10^{-9}s$, $\mu = 2.5 \times 10^{-9}s$. The current waveform at the voltage source is measured to determine the time when the impulse travels back to the feeding point.

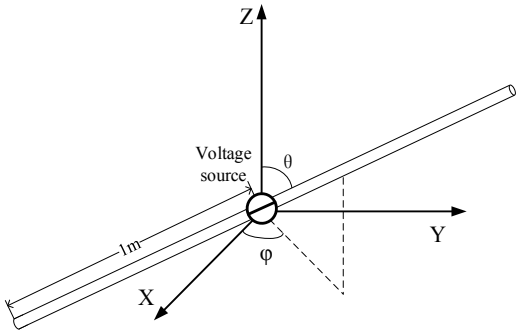

Fig. 8 A dipole structure with an impulse voltage at its feeding point

The conductive arms have two degrees of freedom: θ and φ, as shown in Fig. 8. Both θ and φ are defined respectively as an angle between the conductor and the z axis, and an angle between the conductor projection on the xy plane and

the x axis. θ varies from 0° to 90° with an interval of 10°. φ varies from 0° to 45° with an interval of 15° for the symmetrical geometry.

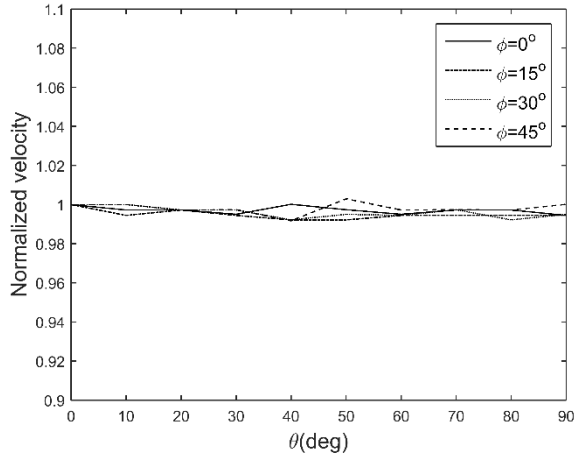

Fig. 9 normalized propagation velocity of the proposed thin-wire model with different inclinations

In the FDTD domain, the cell size is set to be 1 cm, and the time step is 19.2 ps. The perfectly matched layer (PML) absorbing boundary conditions are applied to absorb unwanted wave reflections in six boundaries. In the thin-wire domain, the solid conductor is divided into 201 line segments. The voltage source and current sensor are located in segment 101, i.e. the middle position of the conductor. The propagation velocity of the proposed thin-wire model with different inclinations is shown in Fig. 9. Note, the velocity value is normalized by the result with $\theta = \varphi = 0^\circ$. According to the simulation results, the relative errors of the propagation velocity are less than 1%. Compared with the error of the staircase approximation method [26], which is as large as 14%, the proposed thin-wire model performs well. It is concluded that the proposed model can depict the wave propagation along an inclined direction with a correct velocity.

B. Frequency-dependent loss of solid wire and hollow tube

A lossy conductor is arranged to be in parallel with a perfect ground, as shown in Fig. 10. The conductor is assumed to be infinitely long. One end of this conductor is connected to the ground via a lossless wire and an ideal current source. The current source generates sinusoidal waves of 50 MHz and 100 MHz. Two types of wire structures are tested, including a solid conductor and a hollow tube. Geometric dimensions of these two conductors are shown in Table 1. The conductivity of these conductors is set to be 1e5 S/m for signifying the conductive loss effect. Five current sensors are placed along each of two lossy wire structures at the distance of 10 m, 20 m, 30 m, 40 m and 50 m away from Point P. To test the accuracy of the proposed model under different positions, two configurations of the wire structures are investigated, as shown in Fig.11. In Config. A, Point P is positioned at the corner of the FDTD cell. The lossy wire is located at a height of 0.3 m above the ground. In Config. B, Point P is positioned at the cell center. The lossy wire is then at the height of 0.35 m above the ground. In these two configurations, φ is equal to either 0° or 45°.

Table 1 Geometric dimensions of wire structures

Wire structures	Core radius (mm)	Sheath radius (mm)	Thickness (mm)
Solid conductor	1	\	\
Hollow tube	\	2	0.1
Coaxial conductor	1	2	0.1

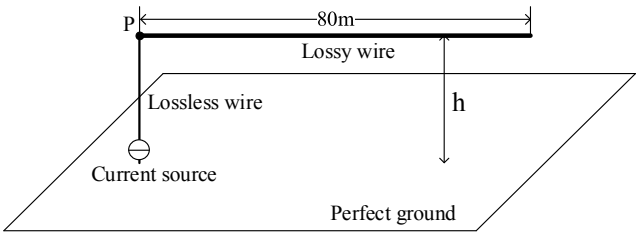

Fig. 10 Configuration of frequency-dependent loss validation with a solid conductor or a hollow tube

Wave propagation over the tested conductor can be analyzed analytically with the transmission line theory (TLT) [36] as the conductor runs in parallel with the ground plane. The peak current along a wire with no reflected wave at angular frequency ω is given by,

$$I(x,t) = I_0 e^{-\alpha x} \sin(\omega t - \beta x), \tag{21}$$

where

$$\alpha = \sqrt{[(\omega^2 LC)^2 + (\omega^2 RC)^2]^{1/2} - \omega^2 LC}\,/\sqrt{2}$$

$$\beta = \sqrt{[(\omega^2 LC)^2 + (\omega^2 RC)^2]^{1/2} + \omega^2 LC}\,/\sqrt{2}$$

C, L and R are the capacitance, inductance and resistance of a traditional transmission line respectively. Both L and R are frequency-dependent, and can be determined using the formulas for surface impedance of round conductors [37].

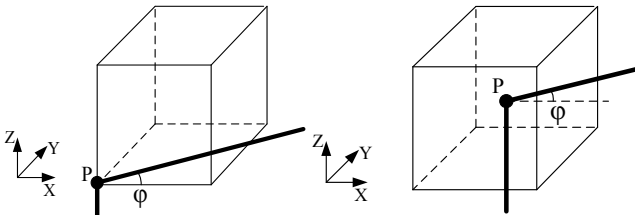

(a) Config. A: cell corner (b) Config. B: cell center

Fig. 11 Location of Point P on the infinitely-long conductor

In the FDTD domain, the cell size and time step are defined as 0.1 m and 9.6225 ps. The working volumes are as large as $860 \times 60 \times 40$ cells for configurations of $\varphi = 0^\circ$ and $620 \times 620 \times 35$ cells for configurations of $\varphi = 45^\circ$. Uniform mesh technique is adopted. Five planes of the PML boundary conditions and one plane of the perfect electrical conductor (PEC) boundary condition are applied on the domain boundaries. In the proposed thin-wire model, the lossy wire is divided into 800 line segments, and the lossless wire is divided into 3 segments in Config. A or 4 segments in Config. B line segments. The frequency-dependent loss is taken into account in the model by applying the 5^{th} order vector fitting technique in time domain analysis.

Simulation results of the solid wire and hollow tube obtained with the proposed thin-wire model and TLT are shown in Table 2 to Table 5. The magnitude of the current wave measured at each location is normalized by the current magnitude at l=10 m. It is noticed that the results obtained from two methods match very well. The averaged relative errors for the solid wire and hollow tube in all configurations

are 0.46% and 1.04% for 50 MHz, and 0.62% and 1.21% for 100 MHz, respectively. This indicates that the proposed thin-wire model is applicable to lossy solid wires and hollow tubes in the time domain.

Table 2 Simulation results for a lossy solid wire (50 MHz)

φ	Method	Current/A				Relative Error
		l=20m	l=30m	l=40m	l=50m	
Config. A: Point P located at the cell corner, h=0.3m						
0^o	Prop.	0.9524	0.9073	0.8640	0.8232	0.75%
	TLT	0.9496	0.9018	0.8564	0.8133	
45^o	Prop.	0.9497	0.9022	0.8570	0.8146	0.08%
	TLT	0.9496	0.9017	0.8563	0.8131	
Config. B: Point P located at the cell center, h=0.35m						
0^o	Prop.	0.9488	0.9005	0.8545	0.8109	0.52%
	TLT	0.9509	0.9042	0.8598	0.8176	
45^o	Prop.	0.9492	0.9008	0.8549	0.8113	0.48%
	TLT	0.9509	0.9042	0.8599	0.8177	

Table 3 Simulation results for a lossy hollow tube (50 MHz)

φ	Method	Current/A				Relative Error
		l=20m	l=30m	l=40m	l=50m	
Config. A: Point P located at the cell corner, h=0.3m						
0^o	Prop.	0.8969	0.8045	0.7217	0.6472	2.78%
	TLT	0.8872	0.7871	0.6983	0.6195	
45^o	Prop.	0.8914	0.7947	0.7086	0.6322	1.23%
	TLT	0.8872	0.7871	0.6983	0.6196	
Config. B: Point P located at the cell center, h=0.35m						
0^o	Prop.	0.8894	0.7913	0.7039	0.6261	0.13%
	TLT	0.8900	0.7921	0.7049	0.6274	
45^o	Prop.	0.9614	0.8555	0.7611	0.6773	0.04%
	TLT	0.9615	0.8557	0.7616	0.6778	

Table 4 Simulation results for a lossy solid wire (100 MHz)

φ	Method	Current/A				Relative Error
		l=20m	l=30m	l=40m	l=50m	
Config. A: Point P located at the cell corner, h=0.3m						
0^o	Prop.	0.9319	0.8686	0.8096	0.7547	1.51%
	TLT	0.9264	0.8584	0.7952	0.7367	
45^o	Prop.	0.9290	0.8599	0.7965	0.7397	0.26%
	TLT	0.9265	0.8583	0.7952	0.7367	
Config. B: Point P located at the cell center, h=0.35m						
0^o	Prop.	0.9266	0.8588	0.7959	0.7376	0.43%
	TLT	0.9283	0.8619	0.8000	0.7426	
45^o	Prop.	0.9256	0.8591	0.7961	0.7380	0.43%
	TLT	0.9283	0.8617	0.8000	0.7427	

Table 5 Simulation results for a lossy hollow tube (100 MHz)

φ	Method	Current/A				Relative Error
		l=20m	l=30m	l=40m	l=50m	
Config. A: Point P located at the cell corner, h=0.3m						
0^o	Prop.	0.8951	0.8014	0.7175	0.6425	2.60%
	TLT	0.8862	0.7852	0.6958	0.6165	
45^o	Prop.	0.8880	0.7904	0.7016	0.6248	0.77%
	TLT	0.8861	0.7852	0.6957	0.6165	
Config. B: Point P located at the cell center, h=0.35m						
0^o	Prop.	0.8870	0.7873	0.6986	0.6201	0.45%
	TLT	0.8889	0.7902	0.7024	0.6244	
45^o	Prop.	0.9330	0.8817	0.8474	0.8101	1.01%
	TLT	0.9462	0.8952	0.8470	0.8014	

C. Coaxial conductors

A lossy coaxial wire structure is tested, as shown in Fig. 12. It runs at the height of 0.3 m above a perfect ground. The length of the wire structure is 20 m. The geometric dimensions are given in Table 1. The conductivity of both core and sheath conductors are 5.96e7 S/m. At one end of the coaxial wire structure, the core is extended further for a distance of 0.5 m horizontally, and then is connected to ground via a lossless wire and an ideal current source. The current source generates a Gaussian impulse, with parameters of $A_0 = 1\,\mathrm{A}$, $\sigma = 9 \times 10^{-10}\,s$ and $\mu = 5 \times 10^{-9}s$. The other end of the coaxial wire structure, the core remains open. The sheath is grounded via lossless wire at the remote end of the structure. There is no electrical connection between the core and sheath of the structure. The radius of the lossless wires is 1 mm. Similar to the arrangement in Section V (B), two configurations for the position of P are considered with $\varphi = 0^\circ$ or $\varphi = 45^\circ$. The current waveforms at the middle point of the core conductor are measured. The results obtained with the proposed model is compared with those from the extended thin-wire model in [21] for validation. In the extended thin-wire model the lossy coaxial conductors are arranged to be in parallel with the FDTD cell edges.

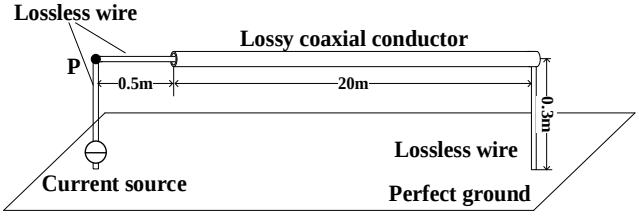

Fig. 12 The configuration of the lossy coaxial conductors

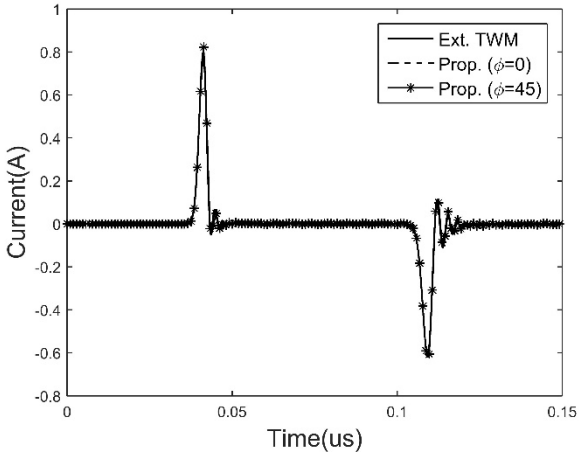

(a) Config A: P at cell corner

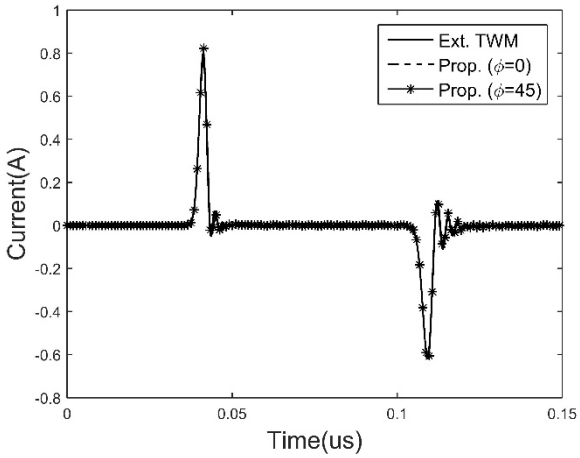

(b) Config B: P at cell center

Fig. 13 Current waveforms at the middle of the core conductor considering the frequency-dependent loss

In the FDTD domain, the cell size and time step are set to be 0.1 m and 9.6225 ps. The working volumes are as large as $255 \times 50 \times 40$ cells for configurations of $\varphi = 0^\circ$ and $200 \times 200 \times 40$ cells for configurations of $\varphi = 45^\circ$. Uniform mesh technique is adopted. The PEC boundary condition is applied at the bottom side of the problem

domain. The PML absorbing boundary conditions are applied on the other sides of the domain. In the thin-wire model, the coaxial wire structure is divided into 200 line segments. The horizontal lossless wire is divided into 5 segments, and the vertical lossless wires are divided into 3 segments in Config. A or 4 segments in Config. B. The 5th order vector fitting technique is adopted.

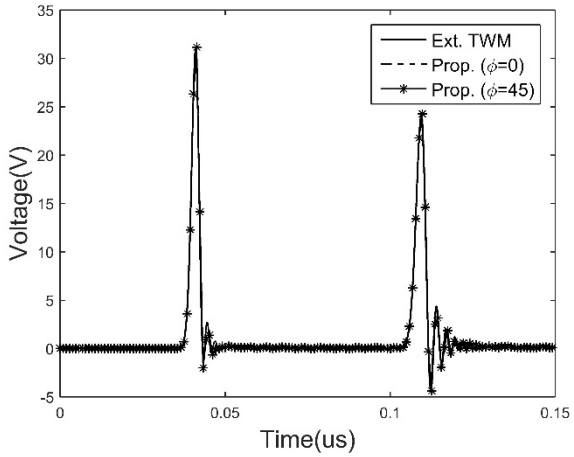

(a) Config A: P at cell corner

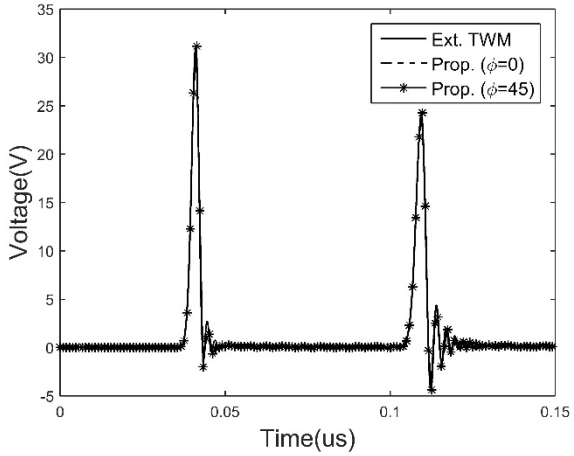

(b) Config B: P at cell center

Fig. 14 Voltage differences between core and sheath conductors at the middle of the cable considering the frequency-dependent loss

In this case, the simulation ran 1 hour ($\varphi = 0^{\circ}$) and 3.5 hours ($\varphi = 45^{\circ}$) in a single core CPU (Inter® Core™ i7-4790 CPU @ 3.60GHz). The current waveforms measured at the middle point of the core conductor under two configurations are shown in Fig. 13. The voltage differences between core and sheath conductors at the middle position of the cable are shown in Fig. 14. In all these cases, current waveforms obtained with two methods match well. The proposed thin-wire model can simulate the inclined coaxial conductors considering frequency-dependent loss with reasonable accuracy.

VI. Conclusions

This paper presented a series of inclined thin-wire models considering frequency-dependent losses for solid conductors, hollow tubes and coaxial conductors with reasonable accuracy. The Bessel functions and the vector fitting technique were adopted to incorporate frequency-dependent parameters of conductors into the time-domain auxiliary equations. Transmission line equations of coaxial conductors were established for wave propagation analysis and linking the wire structure current and conductor currents together. Boundary conditions for the coaxial wire structure were provided as well. The bidirectional coupling between core and sheath conductors was realized with these equations.

Transient simulations in three different cases were performed using the proposed inclined thin-wire models. It is found that wave propagation along inclined lossy conductors is correctly depicted, with the velocity error of less than 1% and the attenuation error of less than 1.5%. The transient currents in the inclined coaxial conductors match well with those obtained from the extended thin-wire models under the assumption that the wire structure is arranged to be in parallel with the FDTD cell edges.

Acknowledgment

The work leading to this paper was supported by grants from the Research Grants Council of the HKSAR (Project No. 152100/17E and 152038/15E) and the Research Committee of the HK PolyU.

Appendix

Consider a coaxial wire structure consists of a core conductor and a sheath conductor withe with radii r_a, r_b and r_c, as illustrated in Fig. 2. By using the definition of the surface electric field over conductor current, surface impedance $Z_{x,y}$ (x=*a, b* or *c,* and y=*co* or *sh*) on surface x contributed by source current in y is represented as [33],

$$Z_{a,co} = \frac{j\omega\mu_{co}}{2\pi R_c}\cdot\frac{I_0(R_c)}{I_1(R_c)}$$

$$Z_{b,co} = j\omega\mu_{sh}\left[\frac{[K_1(R_a)R_a - K_1(R_b)R_b]I_0(R_a)}{2\pi R_a R_b[I_1(R_b)K_1(R_a) - I_1(R_a)K_1(R_b)]} - \frac{[I_1(R_b)R_b - I_1(R_a)R_a]K_0(R_a)}{2\pi R_a R_b[I_1(R_b)K_1(R_a) - I_1(R_a)K_1(R_b)]}\right]$$

$$Z_{b.sh} = j\omega\mu_{sh}\frac{1}{2\pi R_a R_b[I_1(R_b)K_1(R_a) - I_1(R_a)K_1(R_b)]}$$

$$Z_{c.co} = j\omega\mu_{sh}\left[\frac{[K_1(R_a)R_a - K_1(R_b)R_b]I_0(R_b)}{2\pi R_a R_b[I_1(R_b)K_1(R_a) - I_1(R_a)K_1(R_b)]} - \frac{[I_1(R_b)R_b - I_1(R_a)R_a]K_0(R_b)}{2\pi R_a R_b[I_1(R_b)K_1(R_a) - I_1(R_a)K_1(R_b)]}\right]$$

$$Z_{c.sh} = j\omega\mu_{sh}\frac{K_1(R_a)I_0(R_b) + I_1(R_a)K_0(R_b)}{2\pi R_b[I_1(R_b)K_1(R_a) - I_1(R_a)K_1(R_b)]}$$

where $R_x = \gamma r_x$ and $\gamma^2 = j\omega\mu(\sigma + j\omega\epsilon)$. σ is the conductivity of the conductor. I_n is the modified Bessel function of the first kind at order n. A solid conductor or a cylindrical tube is a special case of the coaxial wire structure, in which either the sheath or the core is absent.

References

[1] K. S. Yee, "Numerical solution of initial boundary value problems involving Maxwell's equations in isotropic media," *IEEE Trans. on AP,* vol. 14, pp. 302-307, 1966.

[2] R. Holland and L. Simpson, "Finite-difference analysis of EMP coupling to thin struts and wires," *IEEE Trans. on EMC,* pp. 88-97, 1981.

[3] K. R. Umashankar, A. Taflove, and B. Beker, "Calculation and experimental validation of induced currents on coupled wires in an

arbitrary shaped cavity," *IEEE Trans. on AP,* vol. 35, pp. 1248-1257, 1987.

[4] T. Noda and S. Yokoyama, "Thin wire representation in finite difference time domain surge simulation," *IEEE Trans. on PWRD,* vol. 17, pp. 840-847, 2002.

[5] C. J. Railton, D. L. Paul, I. J. Craddock, and G. S. Hilton, "The treatment of geometrically small structures in FDTD by the modification of assigned material parameters," *IEEE Trans. on AP, on,* vol. 53, pp. 4129-4136, 2005.

[6] R. Xiong, B. Chen, B.-H. Zhou, and C. Gao, "Optimized programs for shaped conductive backfill material of grounding systems based on the FDTD simulations," *IEEE Trans. on PWRD,* vol. 29, pp. 1744-1751, 2014.

[7] B. U. Musa, W. H. Siew, and M. D. Judd, "Computation of transient electromagnetic fields due to switching in high-voltage substations," *IEEE Trans. on PWRD,* vol. 25, pp. 1154-1161, 2010.

[8] A. Tatematsu, S. Moriguchi, and T. Ueda, "Switching Surge Analysis of an EHV Air-Insulated Substation Using the Three-Dimensional FDTD Method," *IEEE Trans. on PWRD,* vol. 33, pp. 2324-2334, 2018.

[9] M. E. Rizk, F. Mahmood, M. Lehtonen, E. A. Badran, and M. H. Abdel-Rahman, "Computation of Peak Lightning-Induced Voltages due to the Typical First and Subsequent Strokes Considering High Ground Resistivity," *IEEE Trans. on PWRD*, vol. 32, pp. 1861-1871, 2016

[10] Q. Zhang, L. Zhang, X. Tang, and J. Gao, "An approximate formula for estimating the peak value of lightning-induced overvoltage considering the stratified conducting ground," *IEEE Trans. on PWRD,* vol. 29, pp. 884-889, 2014.

[11] Y. Baba and V. Rakov, "Voltages induced on an overhead wire by lightning strikes to a nearby tall grounded object," *IEEE Trans. on EMC,* vol. 48, pp. 212-224, 2006.

[12] H. Sumitani, T. Takeshima, Y. Baba, N. Nagaoka, A. Ametani, J. Takami*, et al.*, "3-D FDTD computation of lightning-induced voltages on an overhead two-wire distribution line," *IEEE Trans. on EMC,* vol. 54, pp. 1161-1168, 2012.

[13] A. Tatematsu and T. Noda, "Three-dimensional FDTD calculation of lightning-induced voltages on a multiphase distribution line with the lightning arresters and an overhead shielding wire," *IEEE Trans. on EMC,* vol. 56, pp. 159-167, 2014.

[14] T. H. Thang, Y. Baba, N. Nagaoka, A. Ametani, J. Takami, S. Okabe*, et al.*, "A simplified model of corona discharge on overhead wire for FDTD computations," *IEEE Trans. on EMC,* vol. 54, pp. 585-593, 2012.

[15] T. H. Thang, Y. Baba, N. Nagaoka, A. Ametani, N. Itamoto, and V. A. Rakov, "FDTD simulation of insulator voltages at a lightning-struck tower considering ground-wire corona," *IEEE Trans. on PWRD,* vol. 28, pp. 1635-1642, 2013.

[16] T. Noda, "A tower model for lightning overvoltage studies based on the result of an FDTD simulation," *IEEJ Trans. on Power and Energy,* vol. 127, pp. 379-388, 2007.

[17] T. Noda, A. Tatematsu, and S. Yokoyama, "Improvements of an FDTD-based surge simulation code and its application to the lightning overvoltage calculation of a transmission tower," *Electric power systems research,* vol. 77, pp. 1495-1500, 2007.

[18] T. Noda, "A numerical simulation of transient electromagnetic fields for obtaining the step response of a transmission tower using the FDTD method," *IEEE Trans. on PWRD,* vol. 23, pp. 1262-1263, 2008.

[19] O. Goni, F. Hossain, S. U. Yusuf, M. Rahman, E. Kaneko, and H. Takahashi, "Simulation and experimental analyses of electromagnetic transients behaviors of lightning surge on vertical conductors," *IEEE Trans. on PWRD,* vol. 21, pp. 1778-1786, 2006.

[20] Y. Du, B. Li, and M. Chen, "Surges induced in building electrical systems during a lightning strike," *Electric Power Systems Research,* vol. 139, pp. 68-74, 2016.

[21] Y. Du, B. Li, and M. Chen, "The Extended Thin-Wire Model of Lossy Round Wire Structures for FDTD Simulations," *IEEE Trans. on PWRD,* vol. 32, pp. 2472-2480, 2017.

[22] K. Yamamoto, T. Noda, S. Yokoyama, and A. Ametani, "Experimental and analytical studies of lightning overvoltages in wind turbine generator systems," *Electric Power Systems Research,* vol. 79, pp. 436-442, 2009.

[23] M. Ishii, K. Miyabe, and A. Tatematsu, "Induced voltages and currents on electrical wirings in building directly hit by lightning," *Electric Power Systems Research,* vol. 85, pp. 2-6, 2012.

[24] B. Li, Y. P. Du, and M. Chen, "An FDTD thin wire model for lossy wire structures with non-circular cross section," *IEEE Trans. on PWRD, vol. 33, pp. 3055-3064, 2018.*

[25] A. Tatematsu, "A Technique for Representing Lossy Thin Wires and Coaxial Cables for FDTD-Based Surge Simulations," *IEEE Trans. on EMC,* vol. 60, pp. 705-715, 2018.

[26] T. Noda, R. Yonezawa, S. Yokoyama, and Y. Takahashi, "Error in propagation velocity due to staircase approximation of an inclined thin wire in FDTD surge simulation," *IEEE Trans. on PWRD,* vol. 19, pp. 1913-1918, 2004.

[27] G. Ledfelt, "A stable subcell model for arbitrarily oriented thin wires for the FDTD method," *International Journal of Numerical Modelling: Electronic Networks, Devices and Fields,* vol. 15, pp. 503-515, 2002.

[28] F. Edelvik, "A new technique for accurate and stable modeling of arbitrarily oriented thin wires in the FDTD method," *IEEE Trans. on EMC,* vol. 45, pp. 416-423, 2003.

[29] C. Guiffaut and A. Reineix, "Cartesian shift thin wire formalism in the FDTD method with multiwire junctions," *IEEE Trans. on AP,* vol. 58, pp. 2658-2665, 2010.

[30] C. Guiffaut, A. Reineix, and B. Pecqueux, "New oblique thin wire formalism in the FDTD method with multiwire junctions," *IEEE Trans. on AP,* vol. 60, pp. 1458-1466, 2012.

[31] C. Guiffaut, N. Rouvrais, A. Reineix, and B. Pecqueux, "Insulated Oblique Thin Wire Formalism in the FDTD Method," *IEEE Trans. on EMC,* vol. 59, pp. 1532-1540, 2017.

[32] L. Diaz, C. Miry, P. Baraton, C. Guiffaut, and A. Reineix, "Lightning transient voltages in cables of a large industrial site using a FDTD thin wire model," *Electric Power Systems Research,* vol. 153, pp. 94-103, 2017.

[33] S. A. Schelkunoff, "The electromagnetic theory of coaxial transmission lines and cylindrical shields," *Bell Labs Technical Journal,* vol. 13, pp. 532-579, 1934.

[34] B. Gustavsen, "Improving the pole relocating properties of vector fitting," *IEEE Trans. on PWRD,* vol. 21, pp. 1587-1592, 2006.

[35] B. Gustavsen, "Fast passivity enforcement for pole-residue models by perturbation of residue matrix eigenvalues," *IEEE Trans. on PWRD,* vol. 23, pp. 2278-2285, 2008.

[36] T.-C. Toh, *Electromagnetic Theory for Electromagnetic Compatibility Engineers*: CRC Press, 2013.

[37] L. Xu, Y. Du, and Q. Zhou, "The magnetic field and induced current arising from a cylindrical shell loop with an unbalanced current," *Electric Power Systems Research,* vol. 71, pp. 21-26, 2004.